

# Dry Electrode Manufacturing in a Calender: The Role of Powder Premixing for Electrode Quality and Electrochemical Performance

Andreas Gyulai,\* Werner Bauer, and Helmut Ehrenberg

Cite This: *ACS Appl. Energy Mater.* 2023, 6, 5122–5134

Read Online

ACCESS |



Metrics &amp; More



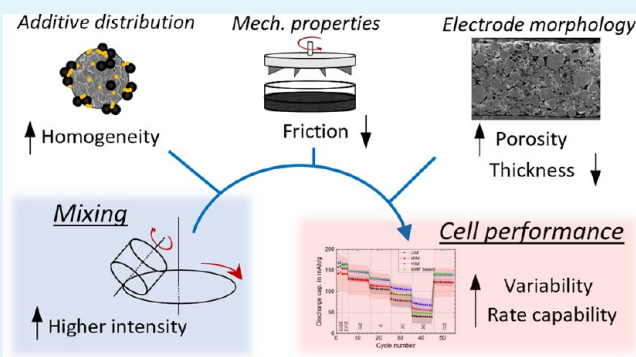
Article Recommendations



Supporting Information

**ABSTRACT:** The dry manufacturing of battery electrodes has the potential to significantly reduce costs and the environmental impact of battery production but deteriorates the electrode quality due to drawbacks in the processability of the materials. By varying the mixing intensity of the powder mixtures, this work investigates the impact of blend homogeneity on the flow properties and the processability of the dry mixtures. Furthermore, the electrochemical performance of dry laminated electrodes made of  $\text{LiNi}_{0.6}\text{Mn}_{0.2}\text{Co}_{0.2}\text{O}_2$  is investigated with respect to their initial mixture homogeneities and compared to slurry-based electrodes. An improvement of the powder flowability is observed for mixtures with a homogeneously distributed PVDF binder, which acts as a temporary lubricant in dry electrode manufacturing due to its ability to shear, resulting also in filament formation. Capacity and rate performance of electrodes made of homogeneous mixtures are the highest with 169 mAh/g at C/20 and 70 mAh/g at 3C compared to 169 and 49 mAh/g for the slurry-based electrodes, respectively. Cyclic voltammetry indicates lower overpotentials for incompletely homogenized electrodes due to the existence of carbon black aggregates that establish better long-range conductivity. Overall, electrodes from highly homogenized powders show the best electrochemical performance in terms of C-rate capability due to their favorable electrode thickness and porosity resulting from better processability in combination with a sufficiently distributed carbon binder domain.

**KEYWORDS:** lithium-ion cathode, calendaring, roll milling, solvent free, powder mixing, powder rheology



## INTRODUCTION

The battery production capacity is increasing worldwide and follows the demand driven by the electrification of the transportation sector and the general shift toward renewable energies, for all of which energy storage solutions are necessary.<sup>1,2</sup> Especially, high voltage battery systems such as lithium-ion batteries (LIB) are needed in electric vehicles (EVs), which accounts for almost 80% of the global LIB demand.<sup>3</sup> Therefore, the production capacity of LIB is expected to increase about 20-fold until 2050.<sup>4</sup> Despite many developments in battery chemistry and manufacturing optimization, electrode coating costs make up 25% of the total battery production costs for EVs.<sup>5</sup> With increasing production capacities, further reductions of the electrode manufacturing costs lead to significant economic advantages, finally resulting in lower costs of the final products, such as EVs, which would strongly enforce consumers shifting to more sustainable technologies.

The state-of-the-art slurry casting process for electrode manufacturing has seen many developments in the past few years to increase product output while minimizing process costs and maintaining the necessary electrode quality.<sup>6–8</sup> Since further optimization proves more and more difficult, alternative

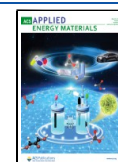
electrode manufacturing processes have been investigated, which have an advantageous process design either concerning product quality and/or production costs.<sup>9–11</sup> One of these alternative approaches is the dry coating of electrodes. By the elimination of the liquid solvents that are typically used in the state-of-the-art process, the processing costs are reduced since the energy-intensive drying step and solvent recovery become obsolete. By this, the electrode production costs can be decreased by 19–22%, which accounts for 1.8–2.6% of the total battery pack cost, not yet including the solvent material costs and the significantly reduced plant space.<sup>12</sup>

For the manufacturing of porous electrodes in a dry process, two variants show promising results and receive attention from the industry to be adapted on a large scale: electrostatic spray coating and roll-to-roll calendaring.<sup>13–16</sup> While the electrostatic spray coating is versatile in terms of electrode

Received: November 28, 2022

Accepted: March 17, 2023

Published: May 5, 2023



characteristics, such as thickness, porosity, and composition, and can produce good quality electrodes, it is challenging to scale up and necessitates rigorous safety measures due to the vaporization of the electrode components, which are most often hazardous and highly explosive when strongly aerated.<sup>14,17</sup> The roll-to-roll calendaring process has the advantage of a simple process design where the battery powders are mixed and consequently compressed to an electrode sheet between two rolls followed by a second calendaring step where the lamination to the current collector takes place.<sup>16</sup> Low equipment, plant space, and energy requirements are needed, and upscaling by numbering up is easy. Challenges yet to overcome by the process are the limited flow properties of the battery materials often leading to inferior electrode quality in terms of electrochemical performance as well as electrode thickness and density homogeneity.<sup>15</sup> Despite a simple process design, the processability of a dry powder mixture depends on a multitude of material and process parameters that are intercorrelated, while material properties and composition must be optimized for their electrochemical performance rather than for processability.

In this work, the manufacturing of porous LIB cathodes with  $\text{LiNi}_{0.6}\text{Mn}_{0.2}\text{Co}_{0.2}\text{O}_2$  (NMC622) as active material (AM) using a two-roll calendaring process is investigated. Special emphasis is laid on the influence of mixing homogeneity as well as deagglomeration and distribution of particles in the powder mixture. For mixtures with different mixing intensities, the processability, flow properties, and electrode morphology are analyzed. Finally, electrochemical performance of the resulting electrodes is determined and compared to state-of-the-art electrodes. The influence of the mixing homogeneity and the unique morphology caused by the dry processing are evaluated.

## THEORY OF CALENDERING

Calendering is the compaction process between two rolls of a roll mill. In battery production, calendaring is commonly used to evenly compact cast electrodes to a desired thickness and porosity. By this, the electric conductivity of the electrodes can be improved and the adhesion to the current collector can be increased.<sup>18</sup> Additionally, the energy density is increasing due to the lower porosity of the electrode layer.

In dry electrode production, calendaring is used for the formation of the electrode in the first place and depending on the process can be repeated to further compress the electrode or to laminate it onto the current collector.<sup>16</sup> Therefore, the aim of the calendaring step is not pure compaction, and the process setup and parameters vary from the common compaction process. The characteristic functions of calendars and the basic mechanical principles concerning the formation of electrodes are presented in this section.

**Calender Functions.** In dry powder calendaring, the powder is fed into the calender gap horizontally or vertically either by gravity or by pressure through, e.g., extruders. Figure 1 displays the process and highlights the main characteristics of the calendaring process, assuming a vertical feed by gravity only.<sup>19</sup>

The compaction process can be separated into two distinct zones, the “feed zone” and the “nip zone”, which are defined by the angles  $\alpha_F$  and  $\alpha_N$ , respectively.<sup>20–23</sup> In the feed zone, the powder transport into the calender gap takes place by the friction between the particles and the roll surface. Powder in the bulk of the feed zone is further carried out into the

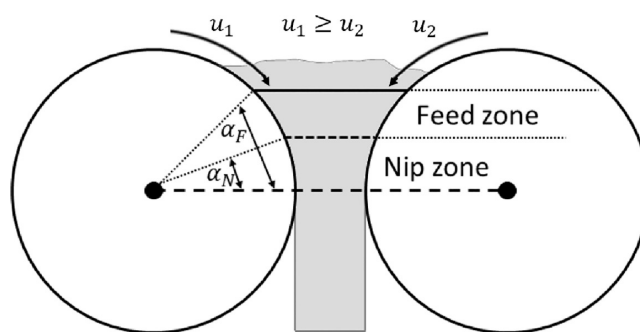


**Figure 1.** Scheme of a vertical powder calendaring process with the distinct gap zones and characteristic parameters.

calender gap by the internal friction of the powder and the speed difference of neighboring particles. This speed difference is created by the roll speeds  $u_1$  and  $u_2$  being unequal, introducing a speed profile into the powder bulk. This relative movement of particles causes the establishment of shear planes approximately parallel to the roll surface at a given angle.<sup>19,24</sup> The angle defining the feed zone is strongly dependent on process and material parameters, which influence friction and shear.

The nip zone, defined by the angle  $\alpha_N$ , is the region of the calender gap where purely compaction takes place.<sup>19,24,25</sup> At the interface between the feed zone and the nip zone, the shearing of the powder reaches zero and the material pressure in the calender gap  $P_M$  increases rapidly with decreasing angles and widths of the calender gap.<sup>19</sup> The pressure in the material is normal to the roll surface, therefore, at low angles almost opposite to the calender pressure. The material pressure can exceed the hydraulic pressure  $P_H$ , thus causing one of the rolls to move on its horizontal axis and opening the calender gap. Therefore, the calender gap width resulting during stationary compaction depends on the frictional and shear behavior of the material system and is not a preset process parameter.<sup>23,24</sup>

Roll surface morphology, roll material properties, working pressure and speed, and roll diameter are relevant parameters in the design of the calender, while particle size and distribution, particle morphology, material composition, state of mixture, and surface chemistry of the powder components are relevant material properties that have to be considered for dry coating.<sup>24</sup> The calculation of the friction conditions and the resulting feed and nip zone angles can be approximated using numerical methods and simplifications<sup>19,26–28</sup> but often lack the precision due to the multitude of parameters, which are difficult to quantify.<sup>24</sup>

**Calender in Dry Electrode Manufacturing.** Meanwhile, in slurry-based electrode manufacturing, post-drying calendaring is used dominantly for compaction purposes and shearing is to be avoided, and in dry electrode manufacturing, strong compaction is undesired, especially for the manufacturing of porous electrodes that are typically soaked with liquid electrolytes in the final cell. In dry electrode manufacturing, strong compaction leads to very dense electrodes and high thicknesses due to immense pressure buildup; thus, the powder becomes unable to flow and shear through the calender gap to form thin and porous electrodes. Additionally, the pressure buildup in solid particulate systems is generally inhomogeneous due to the multitude of point contacts, leading to electrodes with very inhomogeneous thickness and density profiles.<sup>29</sup> To promote electrode formation with higher

porosity and lower thickness, as well as homogeneous density profiles, the feed zone of the calender has to be maximized while the nip zone is minimized to increase the shear zone for an even powder distribution and exert only the minimum necessary compaction to form mechanically stable electrodes.

The calendaring process design changes significantly from the common electrode calendaring and aims to promote shearing of the powder. This can be achieved using calender rolls with specifically designed surface morphology and properties for optimized friction between the roll surface and battery powder. Additionally, shearing can be promoted by calender rolls working at different rotation speeds, leading to a speed profile over the width of the powder bulk. With increasing speed differences between neighboring particles, shear planes in the powder can be promoted. Low working pressures of the calender rolls introduce minimal compaction, thus low normal loads resulting in less particle–particle friction. Finally, powder preparation steps can be applied in the form of specifically designed powder mixing procedures. A homogeneous particle mixture is not only necessary to achieve high homogeneity in resulting electrodes in terms of additive distribution and density profiles but also beneficial for the flowability of the powder during calendaring. Thus, it has a strong impact on the shear behavior and the development of the feed zone.

Beyond changes in the process design, adaptations in the material selection can influence powder flow and shear behavior significantly. Beneficial for the dry manufacturing process are all materials with low cohesion and friction coefficients since these need the lowest shear forces at a given normal load. Therefore, spherical particles with low surface roughness and area are optimal for dry electrode manufacturing in a calender. These properties are often seen in AM particles,<sup>30</sup> which exhibit good flow properties, but the exact opposite is the case for carbon black (CB) additives, which decrease the flowability of the powder blend. Since the desired beneficial particle properties for processing are often disadvantageous for electrochemical performance, a compromise has to be found.<sup>31</sup> Materials such as graphite can be introduced to the particle blend to facilitate shearing in the feed zone due to the plate-like structure of the graphite particles, which are easily sheared apart.<sup>32</sup> Graphite can not only serve as a lubricant in this way but also helps establishing a long-range percolation of the electrically conductive carbon network. Finally, the selection of the binder can strongly improve the shear behavior of the particle blend. By using a binder with very low primary particle size, a fine distribution of the binder on the AM surface can be achieved. With polymers being easily sheared under tension, especially at high temperatures, the binder acts as a strong lubricant at particle–particle contacts, thus promoting shearing in the feed zone.<sup>33</sup>

## METHODS

**Electrode Composition and Materials.** The electrodes are composed of 93.5 w/w%  $\text{LiNi}_{0.6}\text{Mn}_{0.2}\text{Co}_{0.2}\text{O}_2$  (HED NMC622, BASF, Germany) as active material (AM), 3 w% PVDF binder (KYNAR HSV900, Arkema, France), 2.5 w% conductive carbon black (CB) (Super C6S, Imerys, France), and 1 w% conductive graphite (KS6L, Imerys, France). A 17  $\mu\text{m}$ -thick precoated aluminum foil was used as the current collector, with the coating consisting of a sub-micron binder and conductive carbon layer (En'Safe, Armor, France). The primer layer improves electrical contact and adhesion, facilitating the lamination of the dry electrodes to the current collector. For

comparison, solvent-based electrodes of the same composition were prepared using aluminum foil without a primer layer.

**Electrode Manufacturing. Dry Process.** The mixing of each blend was performed in three consecutive steps in a planetary mixer (Thinky ARV-310, Thinky USA Inc., USA). In the first step, only AM and binder were mixed. For the next step, CB was admixed, and in the last mixing step, conductive graphite was further added. The mixing time for each step was 1 min, the revolution speeds are given in Table 1 for each mixing step, and the rotation speed is half the revolution

**Table 1. Mixing Parameters of the Planetary Mixer<sup>a</sup>**

	NMC622 + HSV900 in rpm	NMC622 + C6S in rpm	NMC622 + KS6L in rpm
LIM	500	500	500
MIM	700	1000	500
HIM	1500	2000	1500

<sup>a</sup>One minute mixing time for each setting given in revolution per minute. Rotation per minute is half of the revolution.

speed. In total, three mixtures were prepared with increasing mixing intensity and were further on referred to as the low intensity mixture (LIM), the medium intensity mixture (MIM), and the high intensity mixture (HIM).

The electrodes were formed by calendaring in a two-roll mill in a batch process (GK-300 L, Saueressig, Germany). The calender rolls (200 mm diameter) were heated to 180 °C, and the line load was 230 N/mm at an average feed width of 80 mm. A minimum gap width of 80  $\mu\text{m}$  between the two rolls was ensured by a manual wedge, blocking further gap narrowing. The two rolls were run in opposite directions at different absolute speeds, with the fast roll turning at 0.1, 1, 3, and 5 m/min and the slow roll at 10, 20, and 30% relative to the fast roll, respectively. Therefore, 12 different roll speed settings were used, e.g., the fast roll turning at 5 m/min and the slow roll at 1.5 m/min for the settings of 5 m/min and 30%. For each setting and powder mixture, 10 g of feed was added manually and vertically into the calender gap, producing approximately 100 mm wide and 500 mm long electrode sheets. From the resulting self-supported electrodes, discs of 14 mm diameter were punched and laminated in the second calendaring step to the precoated aluminum foil. For this step, the temperature and pressure remained unchanged, and the roll speed was equal for both rolls at 0.1 m/min. The minimum gap width was set to be 3  $\mu\text{m}$  lower than the sum of aluminum foil thickness and electrode thickness to ensure minimal compression.

**Slurry-Based Process.** Mixing of the slurry was carried out in three steps using a planetary mixer (Thinky ARV-310, Thinky USA Inc., USA). First, the PVDF stock solution in *N*-methyl-2-pyrrolidone (NMP) and the CB was mixed. Second, the AM and graphite were added and homogenized. Third, the slurry was homogenized over 15 min and NMP was added gradually until the slurry reached a solid content of 70 w%.

The slurry was coated onto the plain aluminum foil with a roll-to-roll coater (KTF-S, Matthis, Switzerland) at 0.2 m/min with two drying steps at 80 and 120 °C. The dried coating was calendared to a porosity of approximately 30%, like the dry manufactured electrodes using a lab-scale calender (GKL400, Saueressig, Germany).

**SEM and EDS Imaging.** Scanning electron microscopy (SEM) micrographs were recorded using a field-emission scanning electron microscope (Supra 55, Zeiss, Germany). Energy-dispersive X-ray spectroscopy (EDS) was conducted using an Ultim Extreme silicon drift detector (Oxford Instruments, UK) with an acceleration voltage of 4 kV. Cross sections of the electrodes were prepared with an ion-beam mill (EM TIC3X, Leica Microsystems, Germany) using argon ions at an acceleration voltage of 6.5 kV and 3 mA gun current.

**Powder Resistivity.** A sample of 2 g of each dry powder mixture was filled in an insulating polymer cylinder and contacted vertically by copper pistons. A normal load of 80 N was exerted onto the powder through a piston with a diameter of 24 mm using a static material testing machine (ZwickiLine, ZwickRoell, Germany). The height of

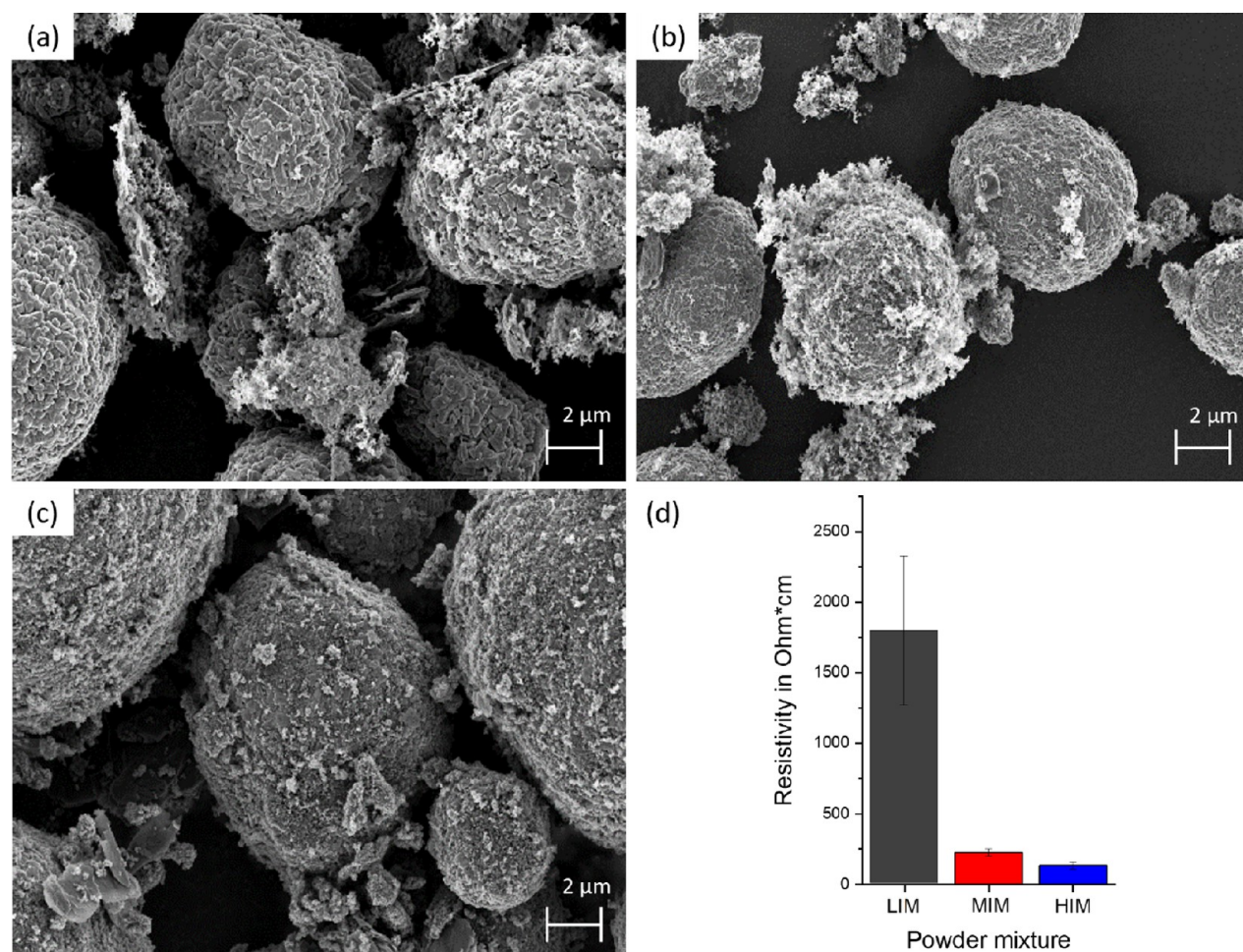


**Figure 2.** Representative SEM images of the (a) LIM, (b) the MIM, and (c) the HIM. (d) Electric resistivity of the corresponding powder mixture bulk at a normal load of 80 N and sample diameter of 24 mm. The scattering of resistivity values is indicated by standard deviations from five independent experiments.

the compressed powder bulk was recorded, and the resistance between the two pistons was measured using a multimeter (Fluke8842A, Fluke, USA). The measurement was repeated five times for each powder mixture. The powders were tested with a DC polarization method to have a purely ohmic and linear current response to potential steps, as shown in Figure S8 in the Supporting Information. Thus, resistivity measurements with the multimeter offer equivalent results.

**Powder Rheology.** The internal friction coefficient of the mixtures was measured with an automated ring shear cell (RST-01, Dietmar-Schulze Schüttgutmesstechnik, Germany) derived by the procedures of a Jenike shear cell and further developed by Schulze.<sup>34</sup> For selected consolidation pressures (5, 50, and 150 kPa), the yield locus was repeatedly measured at room temperature at different normal loads and the effective flow curve was determined. From the angle of the effective flow curve, the angle of internal friction was determined, where the internal friction coefficient was calculated.

**Coin Cell Preparation and Electrochemical Testing.** Punched electrodes with a diameter of 12 mm were dried for 24 h in vacuum at 80 °C (VDL23, Binder GmbH, Germany). Cell assembly was conducted in a glovebox under an argon atmosphere (MB 200B, MBraun, Germany) using CR2032 stainless steel coin cell parts (Hohsen, Japan). A 16.5 mm diameter disc of a glass fiber filter (GF/C, Whatman, USA) was used as the separator, and 200 μL of the LP30 electrolyte (Merck, Germany) was added, thus approximately 18–20 μL/mg. Lithium discs (MTI Corp., Canada) were used as the anode with a total thickness of 1.5 mm. The cells were crimped with a

pressure of 51.7 bar using a compact hydraulic press (MSK-110, MTI Corp., Canada). The coin cells were rested for 24 h before testing.

Cell tests were performed between 3.0 and 4.2 V at a constant temperature of 25 °C (MPG2, BioLogic, France), and 175 mAh/g was used as the reversible capacity for NMC622. Two formation cycles were performed at 0.05C followed by three cycles at 0.1C. Subsequently, 10 cycles were performed at discharge rates of 0.5C, 1C, 2C, 3C, and again 0.5C, while charging rates were symmetrical until 1C. At high discharge rates, charging was performed asymmetrical, remaining at 1C. At C-rates of 0.5C and above, constant current–constant voltage (CCCV) charging was performed, with a cutoff current equal to 50% of the corresponding C-rate.

Long life cycling was done with the same coin cell setup between 3.0 and 4.2 V versus a graphite anode (1:1.2 balanced). First, the same C-rate capability test was performed. Then, long-life cycling consisting of 49 cycles at 1C symmetric charge and discharge followed by one cycle at C/20 in a repeating pattern was performed. For all cycles, CCCV cycling was done with a cutoff current equal to C/20.

Cyclic voltammetry (CV) was performed using the same cell setup and potentiostat from 3 to 4.2 V at 25 °C. After a resting time of 6 h, two formation cycles were performed at a voltage step of 0.017 mV/s followed by three cycles at a voltage step of 0.034 mV/s. Subsequently, 10 cycles were performed at 0.17, 0.68, and 3.4 mV/s. The last 50% of each step response was used for the calculation of the corresponding current.

## RESULTS AND DISCUSSION

**Mixture Homogeneity.** The battery mixtures have been analyzed after the mixing step with respect to the particle distribution of the different components, the degree of deagglomeration of the conductive carbon and the binder, and the homogeneity of the redistribution of the aggregates and primary particles on the active material surface. For a qualitative analysis, SEM imaging has been conducted. A representative image for each mixture is given in Figure 2. To ensure statistical credibility of the representative image, several samples of each mixture were analyzed with a high number of images, and some more are shown in the Supporting Information in Figures S1–S3. Additionally, the electric resistivity of the powder mixtures under a constant normal load was measured for each battery mixture and is shown in Figure 2d.

As seen in the SEM image in Figure 2a, the initial CB and PVDF agglomerate particles are still intact in the LIM, with only a few aggregates occupying the surface of the AM. Since the CB as well as the PVDF is added to the particle blend initially as agglomerates, the impact forces during mixing seem to be insufficient to break up the additive agglomerates. Nevertheless, the additive agglomerates and a few broken aggregates are homogeneously distributed through the particle bed, showing a decent homogenization of the components. In the HIM, both the CB and the PVDF particles have been completely separated to either aggregates or primary particles and are redistributed among the AM surface (Figure 2c). The additives are fixated on and cover the majority but not all of the AM surface, allowing good pathways for ion diffusion and intercalation into the AM. The redistribution of the additives is homogeneous through the mixture, every single AM particle being covered by both CB and PVDF. The MIM is an intermediate between the LIM and HIM, where the additive particles are partially deagglomerated but not homogeneously redistributed over the AM surface. Thus, they are not fixed in position and partly occupy single AM particles while other AM particles remain free of additives. In all mixtures, the graphite is added last, and since it is not consisting of agglomerate particles, it is merely homogeneously distributed in the particle blend and acts as a shearing aid during calendaring.

The measured electric resistivities of the powder blends under a normal load of 176.8 kPa are 1793, 226, and 135 Ohm\*cm for the LIM, MIM, and HIM, respectively (Figure 2d). The resistivity of the LIM is significantly higher compared to the other mixtures, which falls in line with the results of the SEM imaging. The CB agglomerates are mostly intact in the LIM, causing a high local concentration of CB. This prevents the formation of extended conductive pathways through the particle bed at a given concentration of 2.5 w/w% CB, which is insufficient to achieve a good percolation. With advanced deagglomeration achieved for the MIM and HIM, the resistivity significantly decreases. The minor difference between the measured resistivities of the MIM and the HIM is caused by the difference in aggregate redistribution. The more homogeneous redistribution of the CB aggregates over the AM surface in the case of the HIM increases the presence of CB at every particle–particle contact, thus resulting in the best CB percolation. Although the homogeneous distribution of the PVDF binder has an insulating effect, the CB is mingled with the binder, assuring good electric conductivity through the particle bed by forming a sufficient carbon binder network.

**Flow Properties.** The internal friction coefficients of the mixtures have been determined by shear cell measurements at different normal loads at room temperature as described in the Methods section. The results are shown in Figure 3.

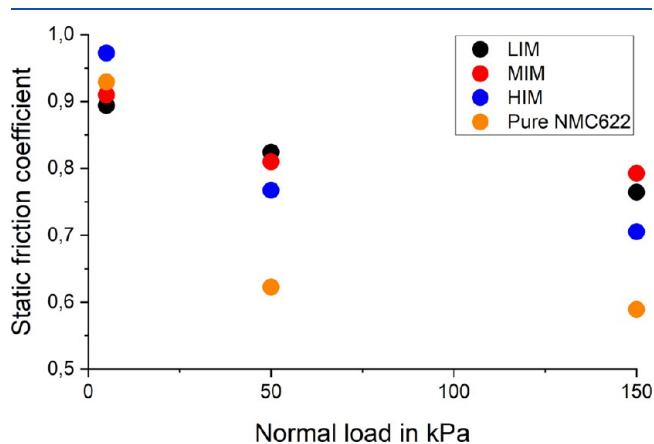


**Figure 3.** Internal friction coefficients of the LIM, MIM, and HIM at different normal loads and room temperature determined by shear cell measurements.

The internal friction of a powder is influenced not only by parameters such as particle size, particle shape, and surface roughness but also material properties, surface charges, crystal structure, and many others.<sup>35,36</sup> The measurement of internal powder friction is done with purely mechanical and relatively simple methods for such a complex concept; therefore, the acting forces are generally summarized into cohesive and mechanical/frictional forces.<sup>34</sup> Cohesive forces are dominant at low normal loads since they incorporate material and surface chemistry specific attractive forces, which are rather independent of the acting normal load. This correlation can be observed in Figure 3 for low normal loads, where internal friction of all material blends is similar to the one of pure NMC622. Since the AM represents the majority of the blend mass and also volume, the cohesion of the NMC622 is the major contribution to the overall friction coefficient, especially for the LIM and MIM with their inhomogeneous distribution of the additives. In the case of the HIM, the friction coefficient is slightly increased by the homogeneously distributed PVDF across the AM surface, which is strongly cohesive due to its high molecular weight, thus strong van der Waals forces and high mechanical interlocking.<sup>37</sup> With increasing normal loads, the cohesion of the materials becomes insignificant compared to the mechanical friction, which is dominantly caused by mechanical interlocking of rough surfaces. The powder blends have a significantly higher friction coefficient than the pure NMC622 caused by the CB and its very high surface area and rough particle morphology. At 50 kPa and even more at 150 kPa normal load, the HIM exerts a significantly lower friction coefficient than the other blends. Now, the homogeneously distributed PVDF acts as a lubricant between the AM particles since the PVDF has the ability to shear under a given shear force. The necessary force needed for polymer shearing can be quite independent on normal load and is attributed more to the polymer structure and the stress development inside the material.<sup>33</sup> Nevertheless, with increasing normal loads, thus AM and CB friction, the polymer more and more acts as a lubricant during shearing, represented by the low friction coefficients of the HIM in Figure 3.

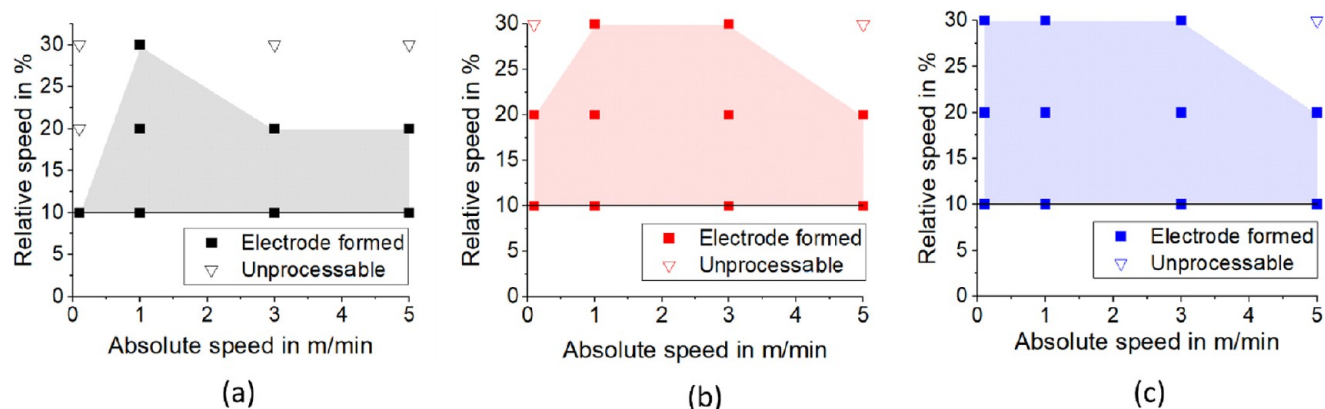


**Figure 4.** Ability of the powder mixtures to form self-supported electrodes at a calender line load of 230 N/mm and different absolute and relative roll speeds: (a) LIM, (b) MIM, and (c) HIM.

It has to be noted that the friction measurements were done at room temperature due to the limitations of the equipment. The measured quantities are based on solid polymer shearing as well as surface properties at room temperature. Although surface properties are not expected to change significantly between room temperature and 180 °C during calendaring, the melting temperature of the PVDF is at approximately 165 °C, thus lower than processing temperature. In the liquid state, the force needed to shear the PVDF is expected to be significantly lower than in the solid state, increasing the role of the binder as a lubricant during calendaring.<sup>38</sup> Additionally, in a liquid state, the molten PVDF shear behavior is even less subject to pressure changes; thus, with increasing normal loads, the lubricating effect is more promoted.<sup>39</sup>

**Processability.** The processability of the mixtures was qualitatively analyzed by their capability of forming self-supported electrodes for a given set of process parameters and quantitatively by the resulting calender roll gap width and final electrode thickness. Calender gap width and electrode thickness both give information about the flowability of the powder mixtures under the applied calender pressure, but the absolute values of these quantities can be significantly different; therefore, both have to be considered individually. Additionally, the gap width can be measured even when no self-supported film could be formed, thus giving information for all applied process parameters. The ability to form self-supported electrodes for a given set of roll-speed parameters is qualitatively displayed in Figure 4.

The LIM is able to form an electrode for the smallest range of process parameters. Without breaking up the additive agglomerates, the binder distribution is insufficient to obtain the necessary cohesion to form a mechanically stable sheet. With increasing shear rate, the processability of the LIM is increasing due to the deagglomeration and shearing of the binder during calendaring, which enhances the distribution of the binder throughout the particle mixture. The MIM was unable to form electrodes for only low shear rates during calendaring. For the used material composition, the deagglomeration and shearing of the binder in the calender gap were enough to obtain the necessary mechanical strength. The HIM was able to form an electrode for most process parameter settings. Due to the deagglomeration of the PVDF and the homogeneous redistribution of its primary particles on the AM surface, good cohesion was achieved through the compaction and melting in the calender gap. Therefore, the HIM could

well form mechanically stable electrode sheets. Although the ability to form mechanically stable electrodes correlates with the binder distribution and increasing shear rates, none of the mixtures was able to form an electrode at 5 m/min and 30% relative speed of the slower roll. This is caused by the nature of the material feeding process into the calender gap. Since the powder is fed manually into the gap zone and no pre-pressure is applied to the resulting powder bulk in the gap, the refilling of the nip zone is caused by gravity and the friction between the particles and the rolls. Meanwhile, at 5 m/min, relative speeds of 10 and 20% for the second roll introduce enough shearing to the powder to continuously refill the nip zone, and at 30%, the refill begins to become inhomogeneous, resulting in gaps and holes in the electrodes. Therefore, a pre-pressure should be applied to the powder feed for faster rotations of either roll by a controlled feeding system. The gap widths during processing of the HIM at given process parameters are shown in Figure 5.

Figure 5a shows the gap width of the calender rolls over the produced electrode length for the HIM at a constant roll speed but different relative speeds. With decreasing speed ratios, thus with increasing speed difference between the rolls, the electrode results in a thinner sheet with a more homogeneous thickness. Due to higher speed differences between the rolls, a higher shear rate is applied on the powder, increasing the feed zone and decreasing the compaction zone, thus shifting the processes in the calender gap away from compression to powder flow. Figure 5b shows the gap width of the HIM over the electrode length at a constant relative speed but at increasing absolute speeds. With increasing absolute roll speed, the gap width is increasing less and is more over the length of the electrode. As long as the rolls are not run at equal speeds, an increase in the absolute roll speed also increases the shear rate; thus, powder flow is promoted.

The processability of the powder mixtures was further analyzed by the resulting electrode thicknesses, which are shown in Figure 6 with the high shear process parameter settings in Figure 6a to the low shear settings in Figure 6c. At the settings with the highest shear rate (10%, 5 m/min; Figure 6a), all three mixtures resulted in electrodes with a similar thickness of approximately 80  $\mu\text{m}$  and a reduction in absolute speed leads to an increase in electrode thickness, especially for the LIM and MIM. The thickness of the HIM remains at approximately 80  $\mu\text{m}$  for all absolute speeds at 10%, except for 0.1 m/min, where it is significantly higher than the thickness of

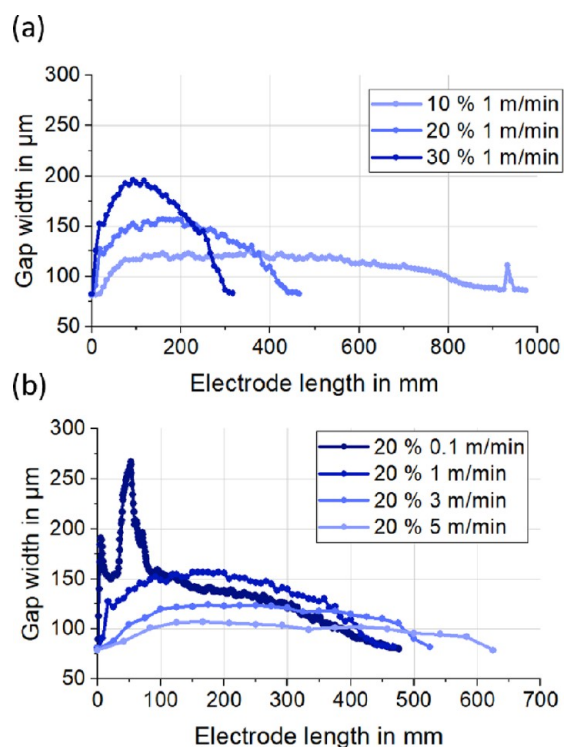


**Figure 5.** Calendar gap width during electrode fabrication over the length of the electrode for 10 g of powder feed. (a) HIM at 1 m/min absolute speed and different relative speeds. (b) HIM at 20% relative speed and different absolute speeds.

the LIM and MIM. This indicates that the HIM is much less processable at this exact parameter setting than the other blends. This result is surprising since at even lower shear parameters at 0.1 m/min absolute speed and 20% relative speed (Figure 6b), the thickness of the HIM is lower. This result was completely reproducible, canceling out the possibility of a measurement error, but no sufficient explanation for this behavior was yet found, thus remaining as the object of further investigation. At medium and low shear parameter settings (Figure 6b,c), a clear trend to thicker electrodes can be observed for decreasing absolute speeds, thus decreasing shear. The LIM and MIM have higher electrode thicknesses over the analyzed parameter range when electrodes could be formed at all. At a relative speed of 30% (Figure 6c), the formation of intact electrodes was almost not possible for the LIM and partly the MIM, indicating that the powder was barely processable due to bad flow behavior and insufficient mechanical stability caused by inhomogeneous binder distribution. This mechanical instability also leads to the inability of the LIM to form electrodes at 5 m/min and 10% (Figure 6a) and at 0.1 m/min and 20% (Figure 6b).

SEM imaging of the laminated electrode's cross sections reveals additive agglomerates and inhomogeneous additive distribution for the LIM, as can be seen in Figure 7a. The MIM cross section reveals significantly fewer and smaller additive agglomerates but shows occasional PVDF filament formation, although the additives are not homogeneously distributed (Figure 7b). The cross sections of the HIM show significant PVDF filament formation and homogeneous distribution of the additives (Figure 7c). The filaments were formed by shearing during calendaring; thus, they mainly stretch in a direction parallel to the established shear planes. The PVDF

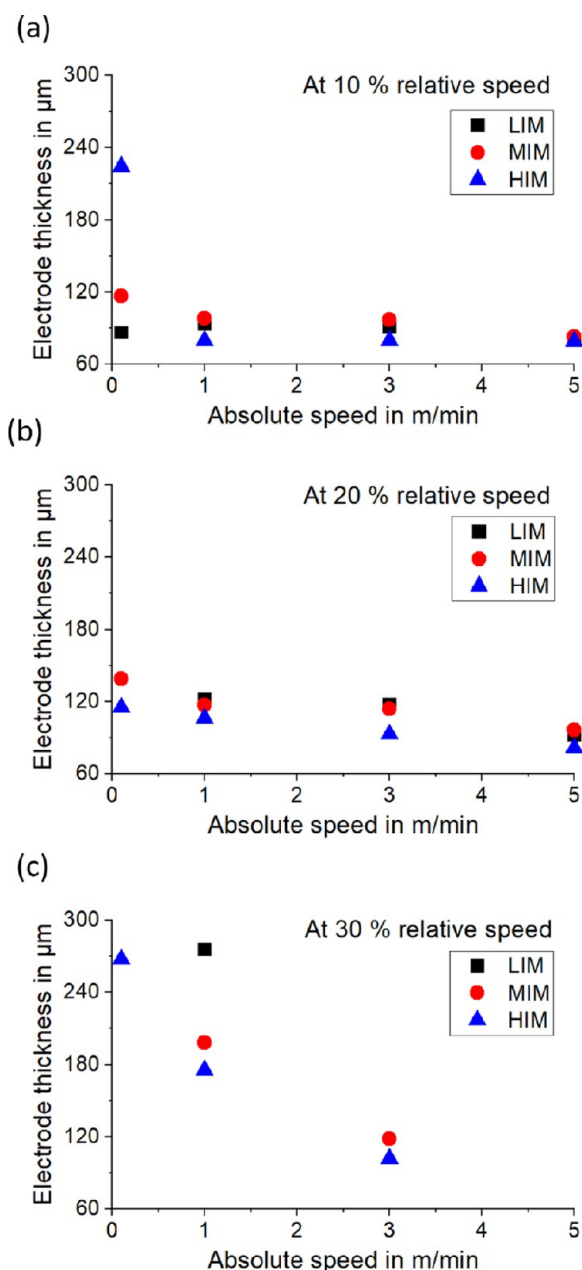


**Figure 6.** Thickness of the resulting electrodes of the mixtures at different absolute and relative speed settings of the calendar rolls and a line load of 230 N/mm: (a) 10% relative speed, (b) 20% relative speed, and (c) 30% relative speed.

filaments are dominantly observed in the HIM and cause the improved processability of this powder blend compared to the LIM and MIM at the given process pressure and roll speeds. The dimensions of the filaments can vary depending on the amount of primary PVDF particles present at the contact points during shearing and can range from tens of nanometers to bundles in the range of micrometers. The deagglomerated carbon black is attached to the PVDF fibrils, ensuring sufficient electric conductivity. The cross section of the NMP-based electrode shows large pores devoid of additives as well as areas densely packed with agglomerates of CB and PVDF (Figure 7d). This kind of inhomogeneous distribution is characteristic for the whole bulk of the NMP-based electrode.

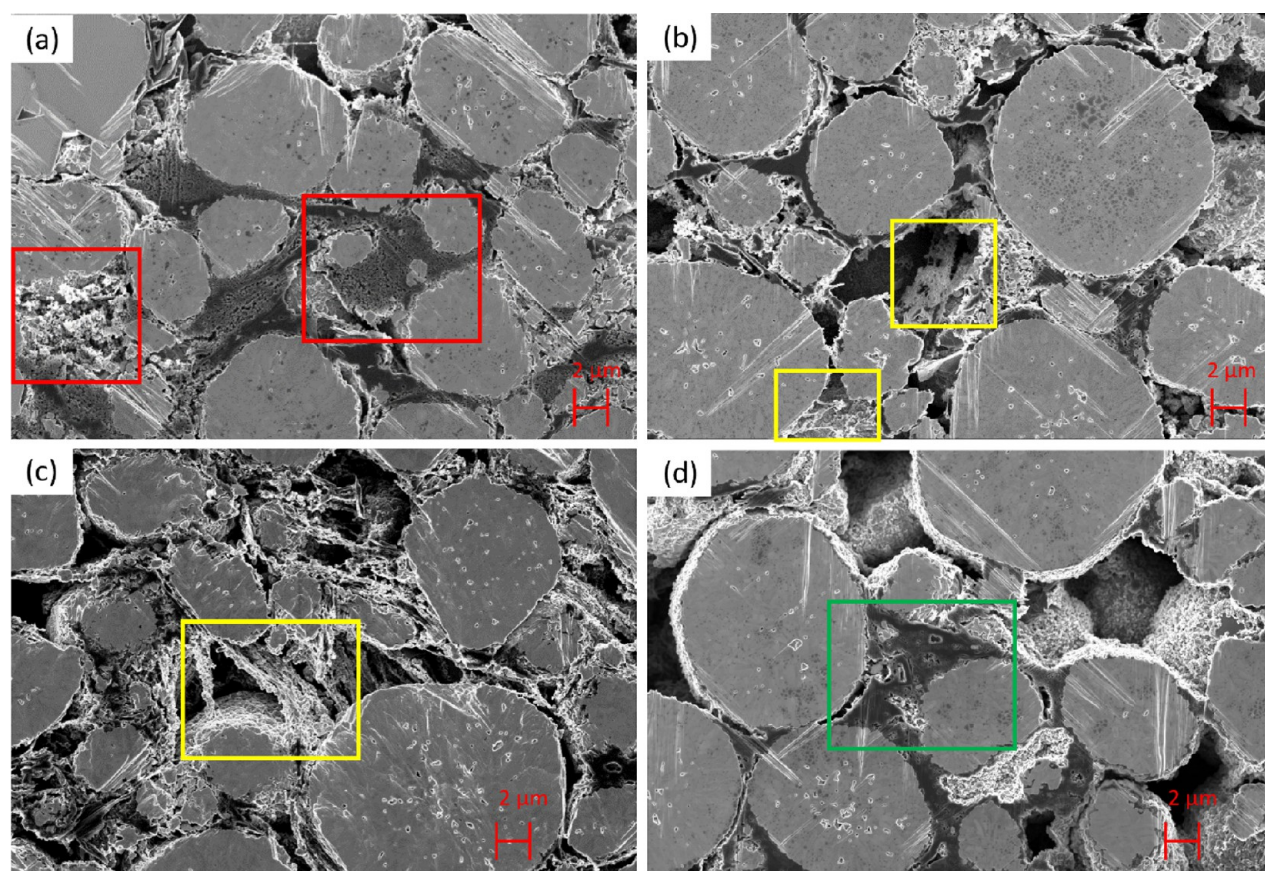


**Figure 7.** SEM imaging of the cross section of the laminated electrodes: (a) LIM, inhomogeneities highlighted in green; (b) MIM, minimal filament formation highlighted in yellow; (c) HIM, filaments highlighted in yellow; (d) NMP-based electrode, PVDF + CB agglomerate highlighted in green.

While the PVDF filament formation during dry calendaring is an advantageous phenomenon for the powder processability and the electrode stability, its final effects on cycling performance are not well investigated yet.

EDS analysis of the cross sections has been conducted to investigate the additive distribution homogeneity in more detail (Figure 8). The carbon signal of the LIM shows big agglomerations of CB, stretching over a wide area of the electrode. Due to the lack of fluorine signal in these areas, it can be concluded that CB has to be the major source of these signals. On the other hand, many interparticle spaces are devoid of carbon and fluorine signals (areas where individual AM particles are difficult to identify). Thus, additive homogeneity is very low. For the MIM in Figure 8b, only smaller CB agglomerations are detected, indicating that the deagglomeration during mixture preparation was translated via the manufacturing process into the electrode layer. Again, interparticle spaces are found that are devoid of both CB and PVDF. Nevertheless, individual AM particles are more easily identified, indicating a slightly higher additive distribution homogeneity. The carbon and fluorine signals of the HIM in Figure 8c are evenly spread through the electrode and can be found distributed around most of the AM particle surface. The AM particles are easily identified, thus indicating a high additive homogeneity. The carbon signal of the NMP-based electrode in Figure 8d shows no clear CB agglomerations, but areas devoid of CB. The fluorine signal is evenly spread through the electrode, indicating a very homogeneous PVDF distribution. The distributions of the CB and PVDF are linked

in a way that PVDF is detected where CB agglomerations are found, but not necessarily vice versa. By this, it is possible that a part of the binder network remains insulating due to a lack of CB caused by its inhomogeneous distribution. The CB distribution of the NMP-based electrode is rather comparable with the LIM or MIM, while the HIM has a significantly more homogeneous CB distribution and a similar PVDF distribution through the electrode bulk.

**Electrochemical Characterization.** Cyclic voltammetry has been performed for all electrodes to analyze the redox potential of the AM (Figure 9a) and the increase in the overpotentials at higher scan rates (Figure 9b).

At a low scan rate (Figure 9a), all electrodes have a peak at around 3.73 V, which is a characteristic value for the Ni redox couple. The shoulder toward higher potentials indicates a split of the redox couple into two steps, namely,  $\text{Ni}^{2+}/\text{Ni}^{3+}$  and  $\text{Ni}^{3+}/\text{Ni}^{4+}$ .<sup>40</sup> At a higher scan rate (Figure 9b), the two redox steps cannot be distinguished due to a broadening of the peaks caused by kinetic limitations. Additionally, the redox peaks during charge and discharge drift apart caused by increasing overpotentials at higher scan rates, which means higher charging currents. While the MIM, HIM, and NMP-based electrode peaks lie at a similar potential, the LIM shows a slightly higher overpotential. Furthermore, the current peaks of the LIM and NMP-based electrode are lower than those of the MIM and HIM, indicating a lower charge and discharge current at the corresponding peak potentials.

The C-rate capability of the dry manufactured electrodes has been compared to a NMP-based electrode with the same

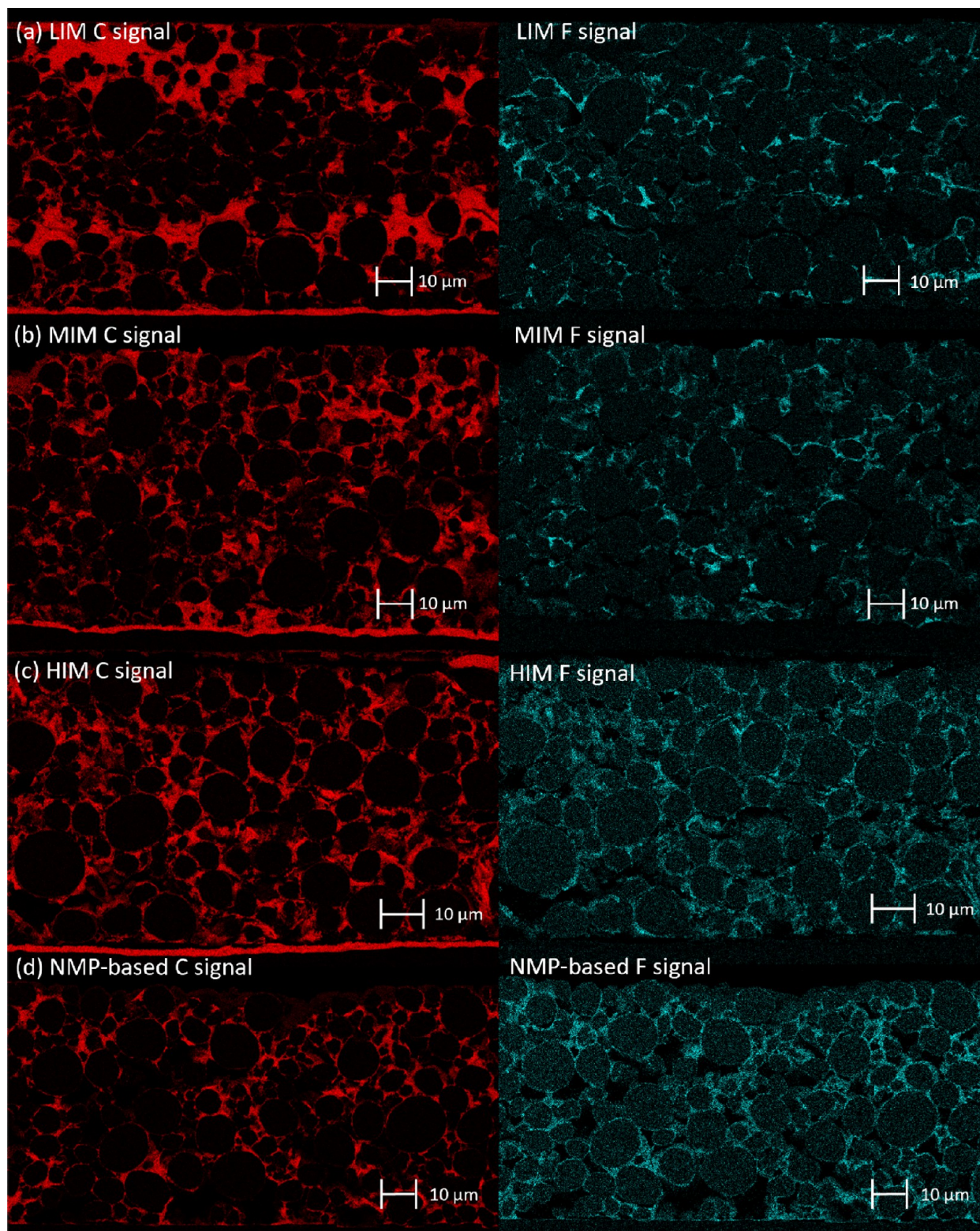


**Figure 8.** EDS analysis of the carbon and fluorine signals of the produced electrode's cross sections: (a) LIM, (b) MIM, (c) HIM, and (d) NMP-based electrode.

composition and relatively similar cell characteristics, such as thickness, porosity, and active mass loading. The results are shown in Figure 10, and the cell characteristics are given in Table 2.

The initial capacity at a C-rate of C/20 spreads from 169 mAh/g for the HIM and the NMP-based electrode to 160

mAh/g for the LIM and 145 mAh/g for the MIM. The capacity of the MIM at low C-rates is significantly lower compared to the other electrodes, and the standard deviation is higher. While the AM of the HIM is homogeneously covered with lubricating PVDF and the LIM has additive agglomerates, which can accommodate certain compression during calender-

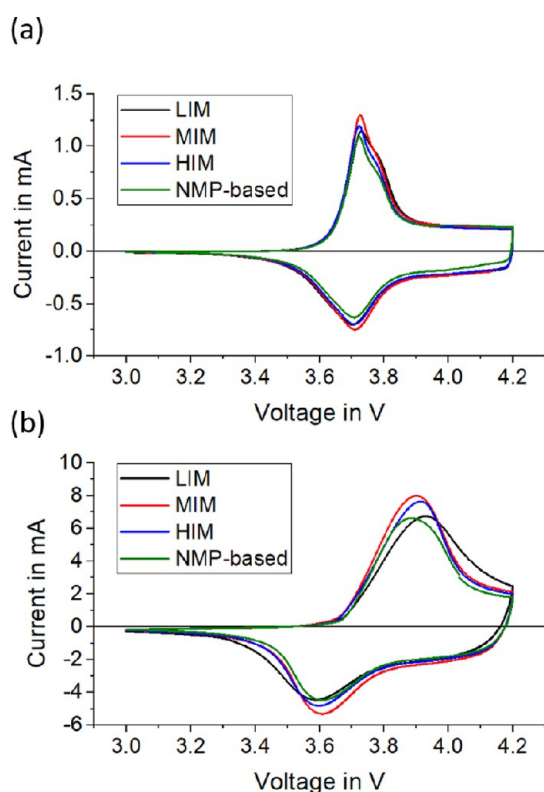


**Figure 9.** Cyclic voltammetry of the dry processed electrodes at scan rates of (a) 0.017 mV/s and (b) 0.17 mV/s.

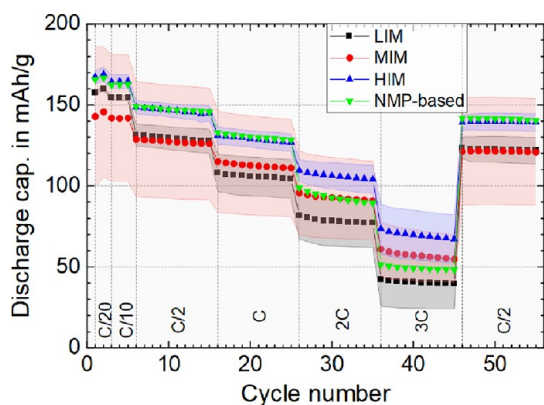


**Figure 10.** C-rate capability test of the dry manufactured electrodes from the investigated powder mixtures compared to a state-of-the-art NMP-based electrode vs lithium anode. Averaged results from five cells of the dry electrodes and two of the NMP-based electrode. The colorful shadowed areas show the standard deviation of the discharge currents.

**Table 2. Electrode Characteristics, Averaged for Five Cells per Electrode Type**

electrode	thickness in $\mu\text{m}$	porosity	AM mass loading in $\text{mg}/\text{cm}^2$
LIM	$86.9 \pm 6.7$	$0.35 \pm 0.02$	$22.3 \pm 1.3$
MIM	$81.7 \pm 1.4$	$0.34 \pm 0.01$	$21.4 \pm 0.8$
HIM	$72.1 \pm 4.4$	$0.30 \pm 0.02$	$20.1 \pm 1.2$
NMP-based	$63.5 \pm 0.1$	$0.30 \pm 0.01$	$17.5 \pm 0.1$

ing, the MIM lacks both. Since the CB is deagglomerated, it occupies the inhomogeneously distributed PVDF, making it

less available to fulfill its role as a binder. Therefore, during the calendaring of the MIM, areas are generated with a lack of binder between the AM particles. These parts of the electrode suffer from very low cohesion and can easily result in crack formation from the stresses during calendaring. After crack formation, small segments of the electrode are poorly connected or even disconnected from the carbon binder domain, resulting in a loss of active material.<sup>41</sup> SEM images showing crack formation due to a lack of binder in certain areas of the electrode are given in the Supporting Information in Figure S5. Cross sections at similar magnifications of the other electrodes are given in Figures S4, S6, and S7 as reference. With increasing C-rates, the MIM outperforms the LIM, having a capacity of 58 mAh/g vs 40 mAh/g at 3C, respectively. Although less AM particles are intact in the MIM, the overpotential at high C-rates is lower due to a better CB deagglomeration, as can be seen in the CV curves in Figure 9.

The HIM has the best C-rate capability with a high initial capacity as well as the highest capacity at 3C with 70 mAh/g. The porosity of the HIM is lower compared to the other electrodes, which is expected to reduce the capacity at high C-rates through ion diffusion limitations.<sup>42</sup> Nevertheless, a lower thickness and the homogeneous distribution of the CB throughout the electrode are beneficial for both the ion diffusion and electronic conductivity, finally resulting in a high capacity in this comparison. At a direct comparison of the HIM and MIM, and after considering the lower initial capacity of the MIM, the rate capabilities of both electrodes are very similar, maintaining a difference approximately as big as the initial capacity difference. Therefore, it is assumed that the deagglomeration of the CB and the resulting high electric conductivity has the major impact on a better C-rate capability in this comparison, while the differences in porosity and thickness between the MIM and HIM are balanced out in terms of ionic conductivity.

The NMP-based electrode has a similar initial capacity as the HIM but has significantly lower capacity retention at higher C-rates, with 49 mAh/g at 3C. Although thickness and mass loading of the NMP-based electrode are lower and porosity is higher than for the HIM, the subpar rate capability of the NMP-based electrode is caused by an unfavorable composition and inhomogeneous CB distribution. While the ratio of CB and PVDF in the selected material composition is optimized for the dry manufacturing, it is disadvantageous for the state-of-the-art slurry casting process, and it has to be taken into account for the direct comparison of the respective electrodes. In a slurry casting process, the use of 2.5 w/w% CB and 3 w/w% PVDF is an unbalanced ratio between the two additives. SEM and EDS analyses show a quite homogeneous distribution of the PVDF, but not of the CB. Either the initial CB agglomerate particles are not deagglomerated sufficiently during slurry preparation or reagglomeration takes place during electrode casting or drying. By this, the added amount of CB is insufficient to provide good conductivity throughout the carbon binder matrix, thus leading to high overpotentials during charge transfer while locally hindering ion diffusion as well. Additionally, the homogeneous distribution of the PVDF on the AM surface can insulate the AM particles, if CB is locally missing. In the dry manufacturing process, even for the HIM, the binder is not as homogeneously distributed as in the slurry casting method since it was not dissolved. Therefore, a part of the used binder is present in small agglomerates or in

the form of filaments and thus is less active in its role not only as the binder but also as the insulator. This effectively tilts the ratio between the CB and the active PVDF in favor of the CB, resulting in lower overpotentials for the HIM and even the MIM.

Finally, the long-life cycling behavior of the produced electrodes has been compared over the length of 800 cycles at a relatively low C-rate of 1C. The results are presented in Figure 11.

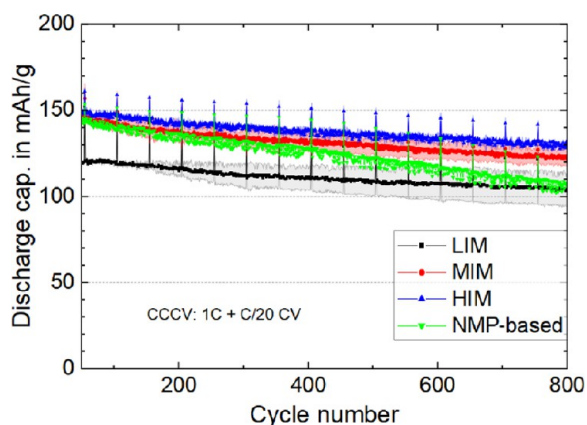


**Figure 11.** Long-life cycling test of the dry manufactured electrodes from the investigated powder mixtures and the NMP-based electrode vs graphite anode. Results for one cell of the NMP-based electrode and the average of two cells for the dry manufactured electrodes.

The discharge capacities of the MIM, HIM, and NMP-based electrodes at the start of the long-life cycling test are very similar, with 149, 145, and 143 mAh/g, respectively. The discharge capacity of the LIM is significantly lower at 120 mAh/g. This behavior translates well from the C-rate capability tests, where the performance of the HIM, NMP-based, and the MIM (after taking the low starting capacity into account) was similar at 1C, while the LIM already shows lower rate capability. The higher absolute values for the measured discharge capacities compared to the C-rate capability test come from the slightly different charging program, where in long life cycles, the cutoff current of the CV charging step is at C/20 instead of C/2 for the C-rate capability test. The curves of the discharge capacity of the dry manufactured electrodes run almost parallel, showing a similar degree of capacity loss with approximately 18, 15, and 14 mAh/g for the HIM, MIM, and LIM, respectively. Due to the minor differences in capacity loss between the dry manufactured electrodes, the same degradation mechanisms are expected. Inhomogeneous additive distribution and binder filamentation seem to have no major influence on the electrode degradation in terms of discharge capacity loss. The NMP-based electrode, although starting at a similar discharge capacity as the HIM and MIM, shows a higher capacity loss during long life cycling of approximately 36 mAh/g. Since additive distribution seems to have no significant impact on the capacity loss, the only other difference between the NMP-based and dry manufactured electrodes is the dissolution of the PVDF. Potentially, the dissolution of the PVDF is disadvantageous compared to the melting of the binder in terms of long-life cycling behavior. However, further research has to be conducted specifically on the differences of the binder after dissolution or melting to

better understand the differences in degradation mechanisms during long life cycling.

## CONCLUSIONS

The understanding of the mechanical processes during dry calendaring can lead to substantial improvements of the process. The impact of process and material parameters on the friction and shear behavior of a powder blend plays a key role for process optimization. Specifically, the mixture homogeneity of a powder blend significantly impacts bulk characteristics such as the internal friction of the powder. By introducing a homogeneously distributed binder that can act as a lubricant during dry electrode manufacturing in a roll mill, shearing during the process was promoted and the processability window could be enhanced. Furthermore, the electrode quality was improved in terms of electrode thickness and capacity retention at higher charge and discharge currents. An even better understanding of the impact of material selection, particle morphology, and particle redistribution during dry mixing is expected to further improve dry electrode manufacturing. Here, it seems possible to reach a level of dry processing of electrodes that can be competitive to slurry-based processes.

## ASSOCIATED CONTENT

### Supporting Information

The Supporting Information is available free of charge at <https://pubs.acs.org/doi/10.1021/acsaem.2c03755>.

SEM micrographs of the mixtures LIM, MIM, and HIM in higher quantity, SEM micrographs of all electrode cross sections, and DC polarization data (PDF)

## AUTHOR INFORMATION

### Corresponding Author

Andreas Gyulai – Karlsruhe Institute of Technology KIT, Institute for Applied Materials (IAM), 76344 Eggenstein-Leopoldshafen, Germany; [orcid.org/0000-0001-7670-4096](https://orcid.org/0000-0001-7670-4096); Email: [Andreas.Gyulai@kit.edu](mailto:Andreas.Gyulai@kit.edu)

### Authors

Werner Bauer – Karlsruhe Institute of Technology KIT, Institute for Applied Materials (IAM), 76344 Eggenstein-Leopoldshafen, Germany; [orcid.org/0000-0002-5923-2426](https://orcid.org/0000-0002-5923-2426)

Helmut Ehrenberg – Karlsruhe Institute of Technology KIT, Institute for Applied Materials (IAM), 76344 Eggenstein-Leopoldshafen, Germany

Complete contact information is available at: <https://pubs.acs.org/doi/10.1021/acsaem.2c03755>

### Author Contributions

A.G. carried out the experimental work and wrote the preliminary manuscript. W.B. and H.E. supervised the project and contributed to interpreting the findings, review, and revision of the final manuscript.

### Funding

This work contributes to the research performed at CELEST (Center for Electrochemical Energy Storage Ulm-Karlsruhe).

### Notes

The authors declare no competing financial interest.

## ACKNOWLEDGMENTS

We thank all our colleagues at the KIT-IAM-ESS who helped to conduct this work through critical reviews and discussions about the content.

## REFERENCES

- (1) Hirsh, H. S.; Li, Y.; Tan, D. H. S.; Zhang, M.; Zhao, E.; Meng, Y. S. Sodium-Ion Batteries Paving the Way for Grid Energy Storage. *Adv. Energy Mater.* **2020**, *10*, 2001274.
- (2) Islam, E. S.; Ahmed, S.; Rousseau, A. Future Battery Material Demand Analysis Based on U.S. Department of Energy R&D Targets. *World Electr. Veh. J.* **2021**, *12*, 90.
- (3) Mackenzie, W. *Global lithium-ion battery capacity to rise five-fold by 2030*; Wood Mackenzie, 2022; <https://www.woodmac.com/press-releases/global-lithium-ion-battery-capacity-to-rise-five-fold-by-2030/>
- (4) Xu, C.; Dai, Q.; Gaines, L.; Hu, M.; Tukker, A.; Steubing, B. Future material demand for automotive lithium-based batteries. *Commun. Mater.* **2020**, *1*, 99.
- (5) Nelson, P. A.; Ahmed, S.; Gallagher, K. G.; Dees, D. W. *Modeling the Performance and Cost of Lithium-Ion Batteries for Electric-Drive Vehicle*; 3rd ed.; Argonne National Laboratory (ANL): Argonne, IL (United States), 2019.
- (6) Zhang, Y. S.; Courtier, N. E.; Zhang, Z.; Liu, K.; Bailey, J. J.; Boyce, A. M.; Richardson, G.; Shearing, P. R.; Kendrick, E.; Brett, D. J. L. A Review of Lithium-Ion Battery Electrode Drying: Mechanisms and Metrology. *Adv. Energy Mater.* **2022**, *12*, 2102233.
- (7) Schmich, R.; Wagner, R.; Hörpel, G.; Placke, T.; Winter, M. Performance and cost of materials for lithium-based rechargeable automotive batteries. *Nat. Energy* **2018**, *3*, 267–278.
- (8) Armand, M.; Axmann, P.; Bresser, D.; Copley, M.; Edström, K.; Ekberg, C.; Guyomard, D.; Lestriez, B.; Novák, P.; Petranikova, M.; Porcher, W.; Trabesinger, S.; Wohlfahrt-Mehrens, M.; Zhang, H. Lithium-ion batteries -Current state of the art and anticipated developments. *J. Power Sources* **2020**, *479*, 228708.
- (9) Hawley, W. B.; Li, J. Electrode manufacturing for lithium-ion batteries—Analysis of current and next generation processing. *J. Energy Storage* **2019**, *25*, No. 100862.
- (10) Bryntesen, S. N.; Strømman, A. H.; Tolstorebrov, I.; Shearing, P. R.; Lamb, J. J.; Stokke Burheim, O. Opportunities for the State-of-the-Art Production of LIB Electrodes—A Review. *Energies* **2021**, *14*, 1406.
- (11) Kwade, A.; Haselrieder, W.; Leithoff, R.; Modlinger, A.; Dietrich, F.; Droeder, K. Current status and challenges for automotive battery production technologies. *Nat. Energy* **2018**, *3*, 290–300.
- (12) Wood, D. L.; Quass, J. D.; Li, J.; Ahmed, S.; Ventola, D.; Daniel, C. Technical and economic analysis of solvent-based lithium-ion electrode drying with water and NMP. *Drying Technol.* **2018**, *36*, 234–244.
- (13) Schällicke, G.; Landwehr, I.; Dinter, A.; Pettinger, K.-H.; Haselrieder, W.; Kwade, A. Solvent-Free Manufacturing of Electrodes for Lithium-Ion Batteries via Electrostatic Coating. *Energy Technol.* **2020**, *8*, 1900309.
- (14) Ludwig, B.; Zheng, Z.; Shou, W.; Wang, Y.; Pan, H. Solvent-Free Manufacturing of Electrodes for Lithium-ion Batteries. *Sci. Rep.* **2016**, *6*, 23150.
- (15) Degen, F.; Krätzig, O. Future in Battery Production: An Extensive Benchmarking of Novel Production Technologies as Guidance for Decision Making in Engineering. *IEEE Trans. Eng. Manage.* **2022**, *1–19*.
- (16) Tschöcke, S.; Althues, H.; Fritsche, D.; Kaskel, S.; Schult, C.; Schumm, B.; Schönherr, K. Verfahren zum Herstellen eines Trockenfilms sowie Trockenfilm und mit dem Trockenfilm beschichtetes Substrat. DE 102017208220 A1, 2018.
- (17) Al-Shroofy, M.; Zhang, Q.; Xu, J.; Chen, T.; Kaur, A. P.; Cheng, Y.-T. Solvent-free dry powder coating process for low-cost manufacturing of  $\text{LiNi}_{1/3}\text{Mn}_{1/3}\text{Co}_{1/3}\text{O}_2$  cathodes in lithium-ion batteries. *J. Power Sources* **2017**, *352*, 187.
- (18) Meyer, C.; Weyhe, M.; Haselrieder, W.; Kwade, A. Heated Calendering of Cathodes for Lithium-Ion Batteries with Varied Carbon Black and Binder Contents. *Energy Technol.* **2020**, *8*, 1900175.
- (19) Lee, R. S.; Schwartz, E. G. An analysis of roll pressure distribution in powder rolling. *Int. J. Powder Metall.* **1967**, *3*, 83–91.
- (20) Daugherty, T. S. Direct roll compacting sheet from particles. *Powder Metall.* **1968**, *11*, 342–357.
- (21) Kurtz, B. E.; Barduhn, A. J. Compacting granular solids. *Chem. Eng. Prog.* **1960**, *56*, 67–73.
- (22) Tracey, V. A. The roll-compaction of metal powders. *Powder Metall.* **1969**, *12*, 598–612.
- (23) Tundermann, J. H.; Singer, A. R. E. The flow of iron powder during roll compaction. *Powder Metall.* **1968**, *11*, 261–294.
- (24) Herrmann, W. *Das Verdichten von Pulvern zwischen zwei Walzen*; Verlag Chemie: Weinheim, 1973.
- (25) Vinogradov, G. A.; Katashinskii, V. P. The angle parameters of the metal-powder rolling process. *Sov. Powder Metall. Met. Ceram.* **1965**, *4*, 722–726.
- (26) Orowan, E. The Calculation of Roll Pressure in Hot and Cold Flat Rolling. *Proc. Inst. Mech. Eng.* **1943**, *150*, 140–167.
- (27) Troost, A. Grundlagen des Bandwalzens. In *Grundlagen der bildsamen Formgebung*; Verlag Stahleisen mbH: Düsseldorf, 1966, 162
- (28) Johanson, J. R. A Rolling Theory for Granular Solids. *J. Appl. Mech.* **1965**, *32*, 842–848.
- (29) Rumpf, H.; Sommer, K.; Steier, K. Mechanismen der Haftkraftverstärkung bei der Partikelhaftung durch plastisches Verformen, Sintern und viskoelastisches Fließen. *Chem. Ing. Tech.* **1976**, *48*, 300–307.
- (30) Lueth, S.; Sauter, U. S.; Bessler, W. G. An Agglomerate Model of Lithium-Ion Battery Cathodes. *J. Electrochem. Soc.* **2016**, *163*, A210–A222.
- (31) Müller, M.; Schneider, L.; Bohn, N.; Binder, J. R.; Bauer, W. Effect of Nanostructured and Open-Porous Particle Morphology on Electrode Processing and Electrochemical Performance of Li-Ion Batteries. *ACS Appl. Energy Mater.* **2021**, *4*, 1993–2003.
- (32) Huai, W.; Zhang, C.; Wen, S. Graphite-based solid lubricant for high-temperature lubrication. *Friction* **2021**, *9*, 1660–1672.
- (33) Dobovšek, I. Some Aspects of Shear Yielding and Emergence of Shear Bands in Solid Polymers. *Acta Phys. Pol., A* **2015**, *128*, 619–624.
- (34) Schulze, D. Flow properties of bulk solids. In *Powders and Bulk Solids: Behavior, Characterization, Storage and Flow*; Schulze, D., Ed.; Springer Berlin Heidelberg: Berlin, Heidelberg, 2008, 35–74.
- (35) Shi, R.; Wang, B.; Yan, Z.; Wang, Z.; Dong, L. Effect of Surface Topography Parameters on Friction and Wear of Random Rough Surface. *Materials* **2019**, *12*, 2762.
- (36) Johnson, K. L. The Mechanics of Adhesion, Deformation and Contamination in Friction. *Tribol. Ser.* **1994**, *27*, 21–33.
- (37) Rodriquez, D.; Kohl, J. G.; Morel, P.; Burrows, K.; Favaro, G.; Root, S. E.; Ramírez, J.; Alkhadra, M. A.; Carpenter, C. W.; Fei, Z.; Boufflet, P.; Heeney, M.; Lipomi, D. J. Measurement of Cohesion and Adhesion of Semiconducting Polymers by Scratch Testing: Effect of Side-Chain Length and Degree of Polymerization. *ACS Macro Lett.* **2018**, *7*, 1003–1009.
- (38) Lenk, R. S. The Influence of Pressure on the Viscosity of Polymer Melts. Viscosity and Molecular Weight. In *Polymer Rheology*; Lenk, R. S., Ed.; Springer Netherlands: Dordrecht, 1978; 31–39, DOI: 10.1007/978-94-010-9666-9\_4.
- (39) Pantani, R.; Gualtieri, A.; Sorrentino, A.; Speranza, V.; Titomanlio, G. Effect of Pressure on the Viscosity of Polymers: Measurements and Relevance in the Injection Molding of Thermoplastics; 2003, <https://www.researchgate.net/publication/235342563>.
- (40) de Biasi, L.; Kondrakov, A. O.; Gefwein, H.; Brezesinski, T.; Hartmann, P.; Janek, J. Between Scylla and Charybdis: Balancing Among Structural Stability and Energy Density of Layered NCM Cathode Materials for Advanced Lithium-Ion Batteries. *J. Phys. Chem. C* **2017**, *121*, 26163–26171.
- (41) Li, T.; Yuan, X.-Z.; Zhang, L.; Song, D.; Shi, K.; Bock, C. Degradation Mechanisms and Mitigation Strategies of Nickel-Rich

NMC-Based Lithium-Ion Batteries. *Electrochem. Energy Rev.* **2020**, *3*, 43–80.

(42) Heubner, C.; Nickol, A.; Seeba, J.; Reuber, S.; Junker, N.; Wolter, M.; Schneider, M.; Michaelis, A. Understanding thickness and porosity effects on the electrochemical performance of LiNi<sub>0.6</sub>Co<sub>0.2</sub>Mn<sub>0.2</sub>O<sub>2</sub>-based cathodes for high energy Li-ion batteries. *J. Power Sources* **2019**, *419*, 119–126.

## Recommended by ACS

### Mitigating Twin Boundary-Induced Cracking for Enhanced Cycling Stability of Layered Cathodes

Xulin Mu, Pengfei Yan, *et al.*

APRIL 20, 2023  
ACS APPLIED ENERGY MATERIALS

READ 

### Regulating Single-Crystal LiNiO<sub>2</sub> Size and Surface Coating toward a High-Capacity Cathode for Lithium-Ion Batteries

Dong-hee Lee, Minkyung Kim, *et al.*

MAY 03, 2023  
ACS APPLIED ENERGY MATERIALS

READ 

### Converting the Liquid Electrolyte of Li Batteries into a Catalyst for CO<sub>2</sub>RR *via* Laser Irradiation

Feihong Ren, Stefano Deabate, *et al.*

JUNE 08, 2023  
ACS APPLIED ENERGY MATERIALS

READ 

### Unraveling the Role of Composite Li<sub>3</sub>PO<sub>4</sub>/ZrO<sub>2</sub> Coatings Prepared by Dry Milling on High Voltage Spinel Cathodes for Lithium-Ion Batteries: Insights into Lattice Strain, T...

Gurbinder Kaur, Byron D. Gates, *et al.*

OCTOBER 27, 2022  
ACS APPLIED ENERGY MATERIALS

READ 

Get More Suggestions >